



LAWRENCE
LIVERMORE
NATIONAL
LABORATORY

Energetics Measurements of Silver Halfraum Targets at the National Ignition Facility

M. J. May, K. B. Fournier, C. G. Brown , W. H. Dunlop ,
J. O. Kane, P. B. Mirkarimi, J. Moody, R. Patterson, M.
Schneider, K. Widmann

September 26, 2013

High Energy Density Physics

Disclaimer

This document was prepared as an account of work sponsored by an agency of the United States government. Neither the United States government nor Lawrence Livermore National Security, LLC, nor any of their employees makes any warranty, expressed or implied, or assumes any legal liability or responsibility for the accuracy, completeness, or usefulness of any information, apparatus, product, or process disclosed, or represents that its use would not infringe privately owned rights. Reference herein to any specific commercial product, process, or service by trade name, trademark, manufacturer, or otherwise does not necessarily constitute or imply its endorsement, recommendation, or favoring by the United States government or Lawrence Livermore National Security, LLC. The views and opinions of authors expressed herein do not necessarily state or reflect those of the United States government or Lawrence Livermore National Security, LLC, and shall not be used for advertising or product endorsement purposes.

Energetics Measurements of Silver Halfraum Targets at the National Ignition Facility

M. J. May, K. B. Fournier, C. G. Brown Jr., W. H. Dunlop, J. O. Kane,
P. B. Mirkarimi, J. Moody, R. Patterson, M. Schneider and K. Widmann

PO Box 808 L260, Lawrence Livermore National Laboratory, Livermore CA 94551.

E. Giraldez

General Atomics, San Diego CA

(Dated: September 10, 2013)

Abstract

The energetics of novel silver halfraum targets are presented from laser experiments at the National Ignition Facility (NIF). Four beams from the NIF laser were used to heat the halfraum targets with ~ 10 kJ of energy in a 1 ns square laser pulse. The silver halfraum targets were spheres 2 mm in diameter with an 800 μm laser entrance hole (LEH). Targets with different spherical wall thicknesses (8 to 16 μm) were characterized. The energetics and the laser coupling to the targets were determined using the NIF X-ray (i.e. Dante and FFLEX spectrometers) and optical backscatter diagnostics (NBI and FABS). The energy coupled into the targets was 0.85 to 0.88 of the total laser energy with a defocused laser spot of 400 μm in diameter and no spatial smoothing of the beams with phase plates. The coupling increased to 0.92 when 400 μm spot size phase plates were used to smooth each of the four lasers beams. The energy losses from the targets were through X-ray radiation and backscatter from laser plasma instabilities (SBS and SRS) from the LEH. As expected the different wall thickness had different levels of burn through emission. The thickest walled target (~ 15.9 μm) had very low radiative losses through the target wall. The thinnest walled targets (~ 8 μm) radiated about 0.2 of the input energy into X-ray emission.

I. INTRODUCTION

High power and high energy lasers are routinely used as energy sources for high energy density (HED) physics experiments. HED experiments include the studying of the properties of materials under extreme conditions [1], the determining of the equation of state (EOS) of materials [2], the development of bright X-ray sources [3] and the producing of a burning fusion plasma for inertial confinement fusion (ICF) [4, 5]. The ICF experiments typically use the laser to heat a Au hohlraum platform [6, 7] to temperatures ~ 300 eV. The emitted X-rays from the hohlraum ablate the surface layer of the ignition capsule. This ablated material through the rocket motor effect creates a pressure that drives the implosion of the ignition capsule. In material properties experiments, the laser energy is converted to pressure using Hohlraum X-rays that drive a graded density piston into the sample material [1]. Alternatively, the laser can directly deposit its energy by directly hitting the back side of the piston [8]. The piston creates a precise pressure wave for the off-Hugoniot loading of the sample under study.

The spherical laser target of the present work is a variant of the hohlraum laser target used in HED experiments. However, instead of having two laser entrance holes, the targets of the present work have only one, giving rise to the name halfraum. Further more, the size of the halfraum targets of the present work are $\sim \frac{4}{3}\pi (1 \text{ mm})^3 \sim 4.1 \text{ mm}^3$, which is 100x smaller than the volume of a typical hohlraum used in the ignition experiment at the NIF [9, 10]. Small halfraums have been studied before at the Omega laser facility [11–13] and at NIF [14, 15]. While those targets were made of gold and had right circular cylindrical geometries, we find similar performance in terms of X-ray drive, backscatter and X-ray burn through from the spherical silver halfraums [16] used in the present work. Recent research has demonstrated improved performance for rugby ball shaped halfraums compared to equivalent sized right circular cylinder hohlraums [17]; although not related to the purpose of this investigation, note that our spherical halfraum is the geometrical limit of this hohlraum design.

In all HED experiments, the target is heated to a hot plasma state by the laser. The laser energy absorbed by the target is converted into either photons (X-rays) or into kinetic energy of the target material, which is partitioned into kinetic energy in both electron and ion distributions. The interaction of the halfraum target with its environment can create

pressure waves that can be tailored in a novel experimental platform that can be used to study shocks or high pressure waves for planetary seismology or in various materials for acoustic or seismic studies. We are currently developing such a pressure and shock platform at the NIF [18].

The expanding halfraum target forms a spherical pressure pulse that can couple directly into the material under study. The material can be either a gas or a solid. The laser pulse is typically several nanoseconds long, which is an instantaneous deposition of energy with respect to the microsecond time scales over which the pressure pulse evolves. The design of the pressure and shock experiments uses four beams from the NIF laser to deposit approximately 10 kilojoules of 3ω laser light in 1 ns into a thin walled (7 - 16 μm) spherical halfraum target made of silver. The pressure or stress waves induced in the gas or solid can be measured by either PDVF or quartz type pressure gauges [18]. In the work presented here, the characterization of the laser target is discussed in detail. Details of the fabrication and metrology of the targets are given in Ref [16]. The details of the novel experimental pressure and shock platform are discussed elsewhere [19].

The characterization of our spherical targets concentrates on determining the energetics and coupling of the laser energy to the target. A large fraction of the incident laser light is absorbed by the target. The absorbed laser light heats the target mainly through inverse bremsstrahlung. A fraction of the absorbed laser energy is converted to X-ray emission. Some of this is radiated out through the thin walls of the halfraum target. Modeling, which is discussed later, predicts that the majority of the absorbed energy is converted into kinetic energy in the halfraum walls within ~ 10 ns. The laser energy that is not converted into kinetic energy is either lost through the laser entrance hole (LEH) in the form of X-rays or reflected and scattered from the target through interactions between the laser field and plasma instabilities [20]. The fraction of the energy partitioned into kinetic energy is determined by subtracting the energy from these energy loss channels from the measured incident laser energy.

A suite of NIF diagnostics was used to record the X-ray and the visible emission from the target during the characterization, or energetics, experiments. The measurements from the diagnostics allow the energetics of the silver halfraum targets to be quantified with high accuracy. These targets needed to be characterized on dedicated shots. In the pressure and shock platform experiments, gas or seismic material surrounds the halfraum and prevents

the X-ray measurements. The time evolution of the absolute X-ray radiant intensity was measured by using the Dante 1 and Dante 2 low resolution spectrometers [21]. The SXI X-ray imagers quantified the location of the X-ray emission [22]. Full-Aperture Backscatter (FABS) [23] and Near Beam Imaging (NBI) [24] systems quantified the incident laser light reflected from the target from laser plasma interactions (LPI). From these measurements, the energy coupled into the targets was determined to be 85 - 88% of the initial laser energy with a defocused laser spot of 400 μm in diameter and no spatial smoothing of the beams with phase plates. The coupling increased to $\sim 92\%$ when 400 μm spot size Continuous Polarization Phase plates (CPPs) were used to smooth the spatial profile of each of the four lasers beams. For the thickest walled target ($\sim 15.9 \mu\text{m}$) very little of the radiation was lost through the walls of the target. The thinnest walled targets ($\sim 8 \mu\text{m}$) radiated about 20% of the input energy into the X-ray.

II. LASER CONFIGURATION

The NIF laser used for these experiments and 192 individual beams in 48 quads mounted in roughly a spherical configuration on the target chamber [25]. The laser system can deposit over a Megajoule of energy into an ignition target in about 10 ns. For these experiments, only four beams or one quad of the available 48 quads was used to deliver ~ 10 kJ of energy in a 1 ns square laser pulse at the 3ω wavelength of 351 nm. NIF was chosen for these experiments due to the energy density and geometric requirements of the pressure and shock experimental platform. The laser energy needs to be delivered in a single narrow cone that minimizes the radiative losses from a large LEH as well as the hydrodynamic perturbations and distortions from a spherical pressure wave in the pressure and shock experimental platform. A NIF quad is currently the only facility that can deliver the required energy in a single and sufficiently narrow cone.

The four beams from Q31B that were used to drive the halfraum targets are located at $\theta=150^\circ$; $\phi=236.25^\circ$ on the NIF target chamber. The measured 1 ns flat-top laser pulses are shown in Figure 1 for all four shots. Power restrictions on the four beams forced a slight energy reduction for the second set of two shots. The laser delivered 10.12, 10.25, 9.53 and 9.29 kJ of energy for NIF shots N110313-001-999, N110313-002-999, N120129-002-999 and N120129-003-999, respectively. (The NIF shot numbers are coded by date. Shot N110313-

001-999 was the first shot on March 13th, 2011. The 999 refers to a full system shot.) The drive energy for all four shots was within 4% of the request, and, as can be seen in the figure, the reproducibility of the pulse shapes was excellent. Please note that the start of the laser pulse occurs about 250 ps before $t = 0$, which occurs at approximately one half maximum of the laser intensity. All NIF diagnostics are cross-timed to this convention, and signals will appear on all the measurements at about 250 ps before $t = 0$.

NIF ICF experiments use CPPs to spatially smooth the high intensity spots in the beam profiles. The high intensity regions in the laser profile are not desirable and tend to increase the backscatter of the laser light. The standard NIF ignition phase plates focus each laser beam to a $1000 \times 1200 \mu\text{m}$ elliptical spot, which is adequate to fit in the ICF hohlraum LEH. These CPP spot sizes are too large for the small target with an $800\mu\text{m}$ LEH, which was needed to meet the energy density requirements and to minimize the radiative losses out of the LEH. Four custom small spot size phase plates were made to produce a spatially uniform laser profile with a $400 \mu\text{m}$ diameter circular spot. The beam intensity with these CPPs is approximately a super Gaussian profile with a power of $n = 4$. The diameter of $400 \mu\text{m}$ encompasses 85% of the energy of each beam. The small spot size was chosen to meet the target alignment requirements ensuring that each laser beam did not clip the LEH. The phase plates could not be delivered in time to be used on the first two shots, N110313-001-999 and N110313-002-999, but were utilized on the second two shots, N120129-002-999 and N120129-003-999. For shots N110313-001-999 and N110313-002-999, the four beams were operated without any CPPs and defocused to create a $400 \mu\text{m}$ round spot at the target's LEH. The laser intensity was $\sim 8 \times 10^{15} \text{ W/cm}^2$ in one beam assuming a spatially uniform beam profile with the CPPs. Without the phase plates, the laser spatial profiles can have significant non-uniformities and regions of very high intensity.

III. HALFRAUM LASER TARGET

A picture of the halfraum laser target is shown in Figure 2. The halfraum target is a hollow silver sphere with a conical cone or skirt. The ball section of the target is 2 mm in diameter, and has a very thin wall on the order of 7 - 16 μm [16]. The ideal target wall thickness was 7 μm for these burn through measurements; however for the shots reported here, the thinnest walled target fielded had a thickness of $\sim 8 \mu\text{m}$. The total mass of

just the silver sphere is ~ 0.93 mg for a $7\text{ }\mu\text{m}$ thick wall. The low target mass was needed to create the desired energy density with the available input laser energy. The spherical target also needed to withstand 1 atmosphere of pressure from the outside. For the pressure and shock experimental platform, the silver ball is the vacuum barrier confining the test atmosphere. Targets with both $15\text{ }\mu\text{m}$ and $8\text{ }\mu\text{m}$ thick walls were pressure tested and successfully supported up to 2 atm of external gas pressure. Silver was mechanically strong enough to withstand the pressure and had a low enough density to meet the desired energy and energy density requirements with a $7 - 16\text{ }\mu\text{m}$ thick wall.

These targets were novel and developmental, and several batches of targets were manufactured in order to get usable targets that met the requirements. To fabricate these targets, the silver is deposited on a mandrel in the shape of the target and back machined to the correct wall thickness. The mandrel is then etched away leaving just the silver target with the desired wall thickness. The first batch was manufactured with an aluminium mandrel. Two of the Al mandrel targets were used for shots N110313-001-999 and N110313-002-999. A second set was manufactured using an aluminium mandrel for the second set of experiments. The thicknesses of the sphere walls were determined by metrologizing the targets with both Focused Ion Beam (FIB) [26] and XRadia measurements [27]. The FIB measurements are destructive and were performed on a test target from a given batch. The FIB images from a target in the first batch did not show any Al residue from the mandrel for shots N110313-001-999 and N110313-002-999. During the FIB analysis of target from the second batch, it was discovered that the interior had a slight Al residue. This residue was a concern so an additional etch was done to remove most of the remaining Al residue layer from the second batch. One of these re-etched Al mandrel targets was shot on N120129-003-999. For a third batch of targets the Al mandrel was replaced with plastic. After etching away the mandrel, these targets did not show any interior plastic residue and one was used for shot N120129-002-999. Modeling suggests that the small amount of mandrel residue on the interior of the sphere had minimal impact on the target energetics.

The energetics of these targets were characterized for a range of wall thicknesses. The manufactured sphere wall thicknesses were slightly thicker than the requested $7\text{ }\mu\text{m}$. The average thicknesses were $12\pm 1.2\text{ }\mu\text{m}$, $15.9\pm 1.3\text{ }\mu\text{m}$, $8.1\pm 0.9\text{ }\mu\text{m}$ and $8.0\pm 0.9\text{ }\mu\text{m}$ for NIF shots N110313-001-999, N110313-002-999, N120129-002-999 and N120129-003-999, respectively. The second two targets were much closer to the ideal thickness. Xradia measurements

indicated that thinnest targets had wall thicknesses of about 10.4 - 10.5 μm at the interface of the skirt and the sphere, 8.1 - 8.9 μm at the equator of the sphere and 6.2 μm thick at the pole opposite to the LEH.

The skirt is also part of the mounting structure to interface the target to the pressure and shock experimental platform. The skirt wall is ~ 2.5 mm tall and has a thickness of ~ 100 μm . The skirt is part of a vacuum channel for the laser beams entering the spherical hohlraum. The LEH is 800 μm and is at the minimum diameter where the sphere region intersects the conical skirt.

The target was aligned in NIF to use quad Q31B by using the tips of a metrologized fiber mounted to the outside of the sphere. An image from the aligned target is shown in Figure 2. The target axis, which is the axis of the skirt, was aligned to be parallel to the Q31B axis. The lasers entered into the conical section of the target and struck the back wall of the silver sphere as shown in Figure 3. The uncertainty in the alignment of the LEH to the laser path was less than 50 μm , which was significantly less than the required ~ 200 μm .

IV. MODELING

The heating of the target by the NIF laser was modeled using the two dimensional axisymmetric radiation hydrodynamics code LASNEX [28, 29], with multigroup detailed configuration accounting (DCA), non-local thermal equilibrium (NLTE) atomic physics and a laser absorption package. The interior of the hohlraum is modeled with a vacuum computational mesh containing very low density hydrogen gas. To model the evolving radiation environment inside the hohlraum while limiting inaccuracy caused by numerical diffusion of mass across mesh lines, the models are run with a nearly Lagrangian mesh (co-moving with the material) during the laser pulse and up until the target temperature and emission decrease significantly. For the later-time phase of the extended runs, the mesh is then run Eulerian (held fixed in the laboratory frame) to avoid tangling of the mesh.

DCA is a super-configuration NLTE collisional-radiative model [30–32]. It describes the plasma in terms of populations of atomic states, calculates transition rates between levels due to interactions with photons and electrons, and follows the time evolution of populations. Transition rates depend on photon spectrum and the electron distribution. Material properties depend on transition rates and population distributions, and populations

can be explicitly time-dependent with non-linear feedback. The photon spectrum depends on material properties through transport. DCA uses a principal quantum number description (super-configurations), screened-hydrogenic energy levels and rates, and 10-20 levels per ionization stage. DCA includes doubly-excited and autoionizing states, tabulated ionization energies and $\Delta n=0$ transitions (for radiative properties). For the population distributions, forward and reverse rates are related by detailed balance.

The evolution of the silver halfraum having a 7 μm thick wall is shown in Figure 4 and Figure 5 by false color plots of electron temperature, T_e , and electron density, n_e . During the first 1 ns while the laser pulse is on, silver plasma is ablated into the halfraum cavity from the inside wall of the halfraum while a radiative (Marshak) wave propagates supersonically into the silver wall. The hottest radiation temperature, $T_r \sim 250$ eV, occurs near the beam spot. During the pulse, electron temperature reaches a maximum of $T_e > 4.5$ keV in a small region of blown-off Ag plasma. In the path traveled by the beams inside the halfraum, electron densities remain below the critical density for resonance absorption, indicating effective absorption of the laser light near the dense wall. By 3.0 ns, a jet of plasma is emerging from the LEH on the halfraum symmetry axis. At this same time, the rear wall of the halfraum has burned through, forming a growing bubble of silver plasma.

V. X-RAY INTENSITY MEASUREMENTS

The time evolution of the X-ray spectral emission was measured by using the NIF Dante spectrometers [21]. A Dante is a low resolution diode spectrometer that is commonly used during laser produced plasma experiments. The radiation from each target is recorded by using 18 separately filtered channels that cover discrete broad X-ray spectral bands between 50 eV to 10 keV with temporal resolutions of ~ 150 ps. Each channel consists of a different set of X-ray filters, mirrors and X-ray diodes (XRDs) optimized to measure a given spectral region. Absolute radiant intensity measurements are possible since all components are absolutely calibrated, and the geometry of the system is known. The spectra and X-ray emission from a given target are determined from the recorded channel signals by using a spectral reconstruction algorithm, typically called an unfold, and the photometric response functions of each channel [33]. Two Dante spectrometers, 1 and 2, were available on the NIF for these experiments. Each had a different view of the target to help determine the

energetics and laser coupling.

The Dante 1 measured the radiant intensity of the X-rays that drive the energetics of the halfraum target. The Dante 1 is positioned on the NIF chamber at $\theta=143^\circ; \phi=274^\circ$ with a view into the target LEH and of the laser deposition region with a 21.6° angle with respect to the target axis (see Figure 3a). The Dante 1 channels were configured to record the expected spectral range from the LEH as given in Table I. The Dante 2 recorded the X-ray radiant intensity emitted through the thin wall of the silver target with a side view of the sphere. The thick cone does not transmit in this X-ray region and shielded the Dante 2 from the drive X-rays measured by the Dante 1. Dante 2 will quantify just the radiation emitted through the walls of the target. The Dante 2 has a view of 124.1° with respect to the target axis (see Figure 3b). Dante 2 is located at $\theta=64^\circ; \phi=350^\circ$ on the NIF chamber. The Dante 2 channels were configured to record the much softer X-rays expected from the thin walls, and with the configuration given in Table II. The Dante configurations were the same (i.e. using the same type filters, XRDs, etc.) for all four of the energetics shots. The components were not changed between the first two and the second two shots and, therefore, each Dante spectrometer had the exact same components.

The time histories of the X-ray radiant intensities from Dante 1 data are shown in Figure 6. During the laser pulse, the laser drive heats the inside of the laser target, and the X-ray emission increases and peaks at 1 ns when the laser pulse ends. The X-ray radiant intensity decreases for several nanoseconds as the halfraum cools and eventually disassembles. The effective peak radiation temperatures, T_r , inside the targets were about 210 - 220 eV for shots N110313-002-999, N120129-002-999 and N120129-003-999. The first shot N110313-001-999 had a T_r of about 239 eV, which is $\sim 10\%$ higher than the other three. For N110313-001-999, the higher drive recorded by the Dante 1 may be a result of more plasma filling at the LEH, which is consistent with the higher levels of backscatter also observed from that shot. This shot may have had poorer laser coupling to the target due to the unsmoothed spatial beam profiles and/or direct irradiation of the LEH region by the laser beams.

Also shown in Figure 6 is the calculated X-ray radiant intensity versus time from the LASNEX simulations for a target with 10.5 kJ of laser drive delivered in a 1 ns square pulse. LASNEX indicated that there should be no measurable difference in the internal radiation environment inside targets having wall thicknesses in the range explored in these

experiments. The side wall does not burn through during the laser pulse for any of the targets, and, therefore, the wall thickness should not affect the LEH emission. All targets had a similar internal radiation temperature and radiation environment except for the target on shot N110313-001-999. The radiant intensity from the first shot was $\sim 3.5\times$ that of the prediction, and the peak radiant intensity from other three shots were about $\sim 2\times$ that of the LASNEX prediction. The difference between the data and the modeling are well outside of the given error bars for the Dante measurements [34]. A similar disagreement exists between the time integrated spectra reconstructed from the Dante 1 data and the spectrum predicted by the LASNEX modeling that are shown in Figure 7. LASNEX predicted a qualitatively similar spectral shape across a broad energy range, but the prediction is much lower in absolute intensity than the Dante 1 spectral reconstruction.

The time histories of the X-ray radiant intensity emitted from the back wall of the targets as recorded by the Dante 2 are shown in Figure 8. The Dante 2 views the X-ray burn through and the laser deposition region at the exterior of the sphere (see Figure 3). The radiation emitted from the back wall of the targets is very weak as expected. The measured radiant intensities for the three different thickness targets have similar but not identical temporal behaviors. One should observe a bright X-ray emission at the laser deposition region that is correlated with the laser pulse hitting the inside of the sphere. This bright emission lasting about 1 ns starting at $t = 0$ is observed for the $15.9\ \mu\text{m}$ and the two $8\ \mu\text{m}$ thick walled targets. The initial bright emission is absent in the Dante 2 traces for the $12\ \mu\text{m}$ thick walled target on shot N110313-001-999. The laser light might not have fully struck the back side of the silver ball, which is consistent with more radiation lost out of the LEH during the laser pulse as seen on the Dante 1 for this shot. In the three shots where this early emission is seen, it decreases immediately after the laser turns off. For all the targets, the back wall emission has a gradual rise starting at 3 - 4 ns as the deposited energy heats more of the target and eventually burns through the wall destroying it. The absolute X-ray radiant intensity is much weaker in the thicker targets since silver is a good X-ray filter in this region. For the first two shots, N110313-001-999 and N110313-002-999, the emission from the back wall was not expected to persist for more than about 10 ns. Therefore, the Dante 2 scopes were configured to record about 13 ns after the laser pulse. This short record length was enough to record only near, if not at, the burn through peak of the X-ray emission. For the $8\ \mu\text{m}$ thick walled targets on the second two shots, N120129-002-999 and

N120129-003-999, the record length of the Dante 2 scopes was doubled to capture more of the late time X-ray emission.

It should be noted that the burn through for the two 8 μm thick walled targets is also seen on the Dante 1 as the very weak second peak at ~ 5 ns in Figure 6. The intensity is very similar to that recorded on Dante 2, which implies that the burn through at this time is isotropic. The burn through was only captured on the two thinnest walled targets since Dante 1 was configured only to record the bright drive emission.

The LASNEX X-ray radiant intensities are shown in Figure 8 for targets having 15 and 7 μm thick walls. As with the Dante 1 predictions, the predictions for Dante 2 from LASNEX do not have great agreement with the experimental measurements. The modeling of the back side of the target could only be run up to ~ 4 ns. The LASNEX simulations in Figure 8 have a similar early time histories to the emission from the 8 and 16 μm thick walled targets. However, the modeling for the thicker walled targets predicts much more radiation should be emitted through the target wall than is observed. The opposite is true for the 7 μm thick walled target, its calculated brightness is much less than that measured by Dante 2. Figure 9 shows the LASNEX predicted spectrum as seen by Dante 2 for a 7 μm thick target. There is also a discrepancy between the predicted LASNEX spectrum for the 7 μm thick walled target and the reconstructed spectra from the Dante 2 shown in Figure 9. The LASNEX prediction is weaker and slightly higher in photon energy than the measured spectra. At the moment we cannot explain why the measured radiant intensities from Dante diverge so significantly from the simulations.

VI. X-RAY IMAGING

Time integrated images were recorded of all four of the laser targets to determine the emitting region of the X-rays. Two pinhole cameras, the Static X-ray Imager-Lower (SXI-L) and the Static X-ray Imager-Upper (SXI-U) [22] were available with different views of the target. The views are shown as wire frames over the recorded images in Figure 10 and 11. Each of the SXIs recorded either 3 or 4 images in the 3 - 5 keV spectral range. Each of the 3 or 4 images had a different filter thickness to maximize the dynamic range of the cameras. The images that are presented here are those that had the best signal to noise.

The SXI-L is located at $\theta=161^\circ; \phi=326^\circ$ with a view of the LEH and laser drive of the

target. The images for shots N110313-001-999 (12 μm) and N110313-002-999 (15.9 μm) that are presented in Figure 10a and b were filtered using 20 μm of Ti and 75 μm of Be. The images for shot N120129-003-999 (8 μm) in Figure 10c and N120129-002-999 were filtered using 25 μm of Ti and 75 μm of Be. The image for N120129-002-999 is not shown but is very similar to the image for shot N120129-003-999. The energy range for these SXI images is dominated by the L-shell emission of silver. The $n = 3 \rightarrow 2$ and $4 \rightarrow 2$ transitions are around 3 - 4 keV and 4 - 5 keV, respectively. This photon energy is higher than that of the peak of the M-shell spectra measured by Dante 1 that is around 1 keV. The total number of counts in the images for N110313-002-999, N120129-002-999 and N120129-003-999 are all very similar and are $\sim 2.0 \times 10^7$, $\sim 1.8 \times 10^7$ and $\sim 1.4 \times 10^7$ digital counts, respectively. The latter two shots have slightly less intensity, which is roughly consistent with the thicker filters on the camera. The emission from the LEH on shot N110313-001-999 is much brighter (by a factor of about 3) in the thinner 12 μm walled target and is $\sim 5.8 \times 10^7$. The difference in intensities as recorded by the SXI-L for the different shots is consistent with the radiant energy recorded by the Dante 1.

The SXI-L images and the T_r 's from Dante 1 can be better understood in the context of the spatial uniformity of the laser beam profiles. The N120129 shots had the 400 μm spot size CPPs installed. The SXI-L images on these shots recorded very uniform LEH emission. The N110313 shots had a defocused laser spot of 400 μm but no phase plates. Shot N110313-002-999 had an intensity similar to that recorded on the 01/29/12 shots but the emission pattern is very non-uniform. Although shot N110313-001-999 had a uniform emission from the LEH, the intensity is greater than the other three shots. These features and intensity variations on the N110313 shots could be due to instabilities in high intensity regions in the unsmoothed beam profiles. These regions of high intensity will increase the backscatter and losses from the LEH and decrease the laser drive absorbed into the target. Also, the unsmoothed beams had broader spatial profile than the beams with the CCPs installed. This could have resulted in more laser irradiation of the target LEH, which caused more rapid LEH closure and contributed to the backscatter. The lack of phase plates does have an effect on the laser coupling and resulting target energetics.

The potential for a mis-aligned target could also have contributed to the non uniform emission in the SXI-L images. The laser could have struck the conical part of the target due to a misalignment in either the laser beams or the target. This was checked from the target

and laser alignment images. The laser pointing error has been determined to be $\pm 15 \mu\text{m}$. The error in the target position was less than $\pm 30 \mu\text{m}$ from that requested. Both of these numbers are very small and within the $\pm 200 \mu\text{m}$ positioning required for these experiments. These errors in the position translate to a change in recorded radiant intensity of 4-5% as seen in the LASNEX modeling below. Target position and laser pointing cannot explain the unexpected target performance.

The SXI-U is located at $\theta=18^\circ; \phi=123^\circ$ with a view of the back side of the spherical ball and recorded images of the target burn through. The SXI-U images in Figure 11a,b and c were filtered with $5 \mu\text{m}$ of Ti, $2 \mu\text{m}$ of Cu and $1 \mu\text{m}$ of polyimide and show a round glow from the backside of each target. As expected, the backside emission is very weak. The images presented are for shots N110313-002-999 ($15.9 \mu\text{m}$), N110313-001-999 ($12 \mu\text{m}$) and 120129-003-999 ($8 \mu\text{m}$). The image recorded on shot 120129-002-999 is very similar to 120129-003-999 and is not shown. The bright central X-ray emission in N120129-003-999 and N120129-002-999 are the laser deposition region on the inner back wall of the target. A diffuse emission around the bright spot in yellow is the diffuse burn through emission from the rest of the silver sphere. The other two images have a barely visible burn through feature. The total number of digital counts in the images from the thin and thick walled were 2.3×10^6 for the $15.9 \mu\text{m}$ wall, 7.2×10^6 for $12 \mu\text{m}$ wall, 3.2×10^7 for $8.1 \mu\text{m}$ wall and 1.8×10^7 for $8.0 \mu\text{m}$ wall. The intensity roughly scales with the thickness of the back wall and is consistent with the Dante 2 measurements.

VII. OPTICAL MEASUREMENTS AND LASER PLASMA INTERACTION

In all laser experiments, a portion of the incident laser light is reflected or backscattered from the target. These reflections are a result of resonant interactions of the laser electric field with plasma instabilities and are mainly scattering from ion-acoustic waves (stimulated Brillouin scattering (SBS)) and from plasma-electron waves (stimulated Raman scattering (SRS)) [20] in the plasma created inside the target. This backscattered laser light can be non-trivial and needs to be quantified for these halfraum targets. Quad 31B was chosen for the energetics shots since it is one of the NIF quads with the FABS [23] and NBI [24] backscatter systems. The FABS system records the light backscattered from the target that is directed into each of the four incident drive beams. These measurements are done in each

beam path by using streaked spectrometers and photometrically calibrated photodiodes, which are optically filtered for each scattering process. Since the scattering is a complex process, a good fraction of the light is scattered outside of the incident beam paths and is recorded by the NBI system. The scattered light is incident on special NBI scatter plates mounted to the NIF target chamber wall surrounding but not blocking the laser beam paths. The reflected laser light hits the scatter plates and is reflected into a set of gated imaging cameras. The cameras are gated so as not to record the direct illumination of the main laser pulse. The set of cameras is appropriately filtered to record the SRS and the SBS emission.

The NBI images are given in Figure 12 for shots N110313-002-999 and N120129-002-999 for both the SRS and the SBS emission. As mentioned, shot N110313-002-999 did not have any CCP in the beams, and N120129-002-999 used the 400 μm CCPs. The NBI reflection plates are the white outline in the images. The four beam paths are the squares in the center of the images. The NBI only measured the reflections on the plates and not in the beam paths. The NBI analysis uses a reconstruction algorithm to interpolate for the regions outside of the reflection plates. It is clear from these images that most of the scattered laser light falls outside of the beam paths for N110313-002-999 but not for N120129-002-999. The NBI signals are much lower for the two shots with the CCPs installed.

The backscattered laser light that did not fall on the NBI plates was reflected back into the laser beam paths and was recorded by the FABS diodes and streak cameras. The power as a function of time recorded by the FABS diodes are given in Figure 13 for the same two shots shown in Figure 12. The backscatter recorded by the FABS in the SRS channel is much greater than that in the SBS channel. The SRS for N110313-002-999 increases steadily until the laser turns off. The SRS for N120129-002-999 has some indication of increasing but the data does not have high signal to noise. The SBS emission for both shots increase to a plateau around 0.2 - 0.4 ns and then increases again to a peak at about 0.7 ns. The increasing SBS and SRS emission indicates that the target is starting to fill with plasma. The FABS diodes are mainly used to measure the backscatter power, the structure on the FABS diodes is better understood by looking at the streak camera data discussed below. The total backscatter power determined from both the FABS diodes and NBI measurements are give in table III. The effect of smoothing the laser profiles with the CPPs is significant. The dominant SRS channel is decreased by a factor of 2 - 3. The SBS channel backscatter decreased by at least a factor of 5.

The SRS and SBS streak camera data from the FABS are given in Figure 14 for shots N110313-002-999 and N120129-003-999. The white traces in the images are the time history of the laser pulse. The SRS emission should be between 550 - 650 nm, which is a red shift of about 300 nm from the 3ω laser wavelength. This red shift is associated with backscatter off of an electron density of $n_e/n_{crit} \sim 0.1$. The SRS emission is very weak for the first half of each shot and increases in the second half of the laser pulse. This is consistent with the FABS SRS diodes plotted in Figure 13 and the LASNEX simulations in Figure 6 and 7. For the first 0.5 ns of the laser pulse, there is very little plasma predicted to have filled the inside of the silver ball. Most of the plasma will be right at the laser deposition region, which means a very small path length for the laser to traverse. As the laser heats the back wall, it also starts to ablate some of the wall material around the LEH. Between the 0.5 to 1.0 ns the majority of the inside of the target ball is at about $n_e/n_{crit} \sim 0.1$. Therefore, the backscatter gain path length increases significantly. The SRS recorded on N120129-003-999 has a distinct emission at 570 nm, which is indicative of a single backscatter region. N110313-002-999 has a much broader spectral emission than N120129-003-999. The laser is scattering off of a region of much less uniform density. The SXI-L image on N110313-002-999 has non-uniform emission at the LEH, this implies hot spots and filamentation in the beam and is consistent with higher backscatter. The plasma filling of the target is more uniform with the CPPs installed.

The SBS spectra are plotted in Figure 14b and d for the shots N110313-002-999 and N120129-003-999, respectively. The backscattered emission from the ions typically emit near the NIF 3ω wavelength of 351 nm, which is the central wavelength in the figures. The shift in the wavelength is dependent upon both the Doppler shift from the plasma drift velocity and the plasma electron temperature. For shot N110313-002-999, the backscatter emission at the beginning of the laser pulse starts at the principal wavelength of the laser and is blue shifted (negative $\delta\lambda$) since the heated silver plasma supersonically expands away from the back wall of the target. The plasma is significantly accelerated away from the back wall since the blue shift and, thus, particle velocity is increasing with time. The spectrum from shot N120129-003-999 is slightly blue shifted and remains constant as a function of time. There is much less acceleration of the plasma, and the expansion is much more gradual and controlled with CPPs. After the first 0.5 ns of the laser pulse, the LEH of the silver ball in shot N110313-002-999 is likely filling with hot plasma and starting to close. This higher

temperature plasma at the LEH is seen as red shifted backscattered light starting at 0.5 ns in the figure. The emission is fairly narrow in wavelength indicating a uniform temperature plasma. The backscatter shifts to the blue slightly, which is due to the LEH plasma escaping the target. The LEH closure is also apparent in the FABS diode signals seen in Figure 13. After about 0.7 ns the diode SBS emission decreases just before the peak in the diode SRS emission. At this time the $n_e/n_{crit} \sim 0.1$ surface has reached the LEH, thus, reducing the transmission of the laser into the target and reducing the SBS emission from the plasma inside the sphere. The FABS spectra for N120129-003-999 (and N120129-003-999) do not show this second emission feature around the LEH. Therefore, plasma has not yet started to fill the LEH.

VIII. FILTER FLUORESCER - HARD X-RAY EMISSION

The hard X-ray spectra ($h\nu > 10$ keV) are measured with the filter-fluorescer diagnostic system, FFLEX [35, 36]. Each of the 10 FFLEX channels are configured to measure a given hard X-ray energy with a narrow spectral window. The lowest and highest energy channels record X-rays around ~ 20 and ~ 240 keV, respectively. Photons from laser driven target are collimated and pass through a vacuum window. These photons are filtered with an edge filter that is just above the fluorescence edge of the fluorescer foil. The filtered X-rays are absorbed by a K-shell fluorescer foil. The narrow energy range of each channel is defined by the filter and fluorescer absorption edges. The emitted photons from the fluorescer foil are filtered to select just the fluorescer lines that are converted to visible light in a scintillator at the input of a photomultiplier tube detector. In the present configuration the low energy X-rays are limited by the NIF vacuum window thickness requirements. The FFLEX is operated in air and does not share NIF target chamber vacuum.

Figure 15 shows the fit spectra from the ten FFLEX channels for the four target shots. The hard X-ray data were fit with a two-temperature Maxwell-Boltzmann function. The two temperatures from the fits and the total X-ray energy found by integrating the two-temperature spectral reconstruction are listed in Table III for the four shots in this campaign. The lower electron temperatures were very similar for all shots between 2.6 - 3.1 keV. The higher electron temperature components were between 35 - 45 keV. The thicker walled targets had about 10 to 20 J of energy in hard X-rays, whereas the two thin walled targets

with CCPs had a about 45 J of hard X-ray emission. The mechanism for the hard X-ray production is, most likely, the slowing of high-energy electrons on the positively charged Ag ions in the target plasma. The hot electrons are likely produced by the resonant scattering of the laser light from plasma electron waves.

IX. TARGET ENERGETICS

The energetics and laser coupling into these silver targets has been quantified by using the data recorded by the suite of NIF diagnostics. The coupled energy into the laser target is defined as the total laser input energy less the loss mechanisms. The major energy loss mechanisms include the X-rays and the backscattered visible light emitted from the target LEH and the hard X-rays lost in 4π from the target. The laser energy coupled into the target will be partitioned into two forms: the kinetic energy of the particles and the X-rays inside the target, which eventually burn through as the target disassembles. The energy not measured in the form of these burn through X-rays is assumed to have all been converted to kinetic energy in the target material. The energy partitioning and coupling determined from the NIF diagnostics are summarized in Table III for all four shots that were characterized during the energetics campaign on NIF.

One of the largest channels for energy lost from the target was from X-rays emitted through the LEH. The total radiant energy (J/sr) measured from Dante 1 is summarized in the table for each of the targets. These values are the sum over photon energy and 0-10 ns, the time during the recorded X-ray emission. Each Dante recorded the emission from the laser target at only a single angle. The LASNEX simulations predicted that the X-ray emission did vary significantly as a function of viewing angle with respect to the target. The angular dependence predicted by the LASNEX modeling is plotted in Figure 16 for the 7 μm target. The Dante 1 view, Dante 2 view and cone wall angular positions are indicated in the figure. The drive emission from the LEH as viewed by Dante 1 should be independent of the wall thickness and only depend on laser coupling. The absolute intensity of the burn through will of course change with the wall thickness. For this analysis, the predicted relative variation as a function of angle from the target wall is assumed to not change significantly with varying wall thickness. To determine the total drive loss and burn through from each of the targets, the recorded radiant intensity from each Dante is combined with the simulated

angular dependence from LASNEX. For each target and Dante, the LASNEX prediction is scaled to the measured radiant intensity for each Dante at its viewing angle. The scaled LASNEX curve is then summed over the appropriate solid angle geometry to determine the total emitted energy. The total X-rays drive losses from the LEH are 500 to 800 J or about 5 to 8% of the total input laser energy.

The other significant loss of laser energy is due to the backscatter of laser light. For the two targets without CCPs, the backscatter emission was roughly or 650 to 750 J and equal to the measured X-ray losses from the LEH. The backscatter dropped significantly with the installation of the CCPs and was reduced to below 200 J. The final energy loss from the targets will be from hard X-rays ($E > 10$ keV). This emission is assumed to be isotropic into 4π . The total amount of energy in the hard X-ray part of the spectrum is small compared to the losses measured from the X-ray and optical backscatter. It is reported here for completeness. The total coupling of the laser is on the order of 0.85 - 0.88 for both targets without CCPs. When the CCPs were installed, the coupling increased to about 0.92. This is excellent coupling, and provides the energy source that will drive the pressure and shocks in the pressure and shock experimental platform.

The coupled energy is partitioned into thermal/kinetic energy in the expansion of the target material and radiation burn through from the thin wall of the sphere. The total losses from the burn through measured by Dante 2 are given in Table III. The total X-ray burn through energy from the target was determined in a similar manner, as for the Dante 1 drive measurements describe above. The Dante 2 measurements from the back side of the target only recorded up to 13 ns for the first two target shots. Only a fraction of the total wall emission from the target is emitted by this time. These burn through emission estimates are lower limits and are probably low by a factor of 2 to 3. Even so, the total energy lost for the thick wall targets is very small. The Dante record length was increased to 50 ns for the last two target shots. For these shots the back wall emission is down about a factor of ten from the peak at the end of the Dante 2 record. Therefore, the estimated total burn through is fairly accurate. The burn through energy is, as expected, a function of the wall thickness. For the thickness target (15.9 μm thick) the total burn through energy was very small and ~ 4.0 J. About 91 J of X-ray energy burned through for the 12 μm thick target. The most energy was lost with the thinnest target and was ~ 0.2 of the input energy or 1500 to 2000 J of energy.

X. DISCUSSION

As mentioned, our silver halfraum targets are a variant of the gold hohlraum and halfraum laser targets that are commonly used in HED experiments. The performance of gold halfraums have been determined in many NIF experiments. The effects of halfraum target size and the laser power are discussed in the references [37, 38] for a similar configuration and parameter space explored for our Ag targets. For the work presented in the references, the gold halfraum targets varied in radii from 0.28 to 1.2 mm and were heated using four beams from one quad of the NIF laser. The laser energy varied from 7 to 17 kJ with square pulses of 1.1 to 9 ns. The laser power varied from 2 to 9 TW.

The Au halfraum results (solid points) from the references are summarized in Figure 17. The measured T_{rad} and the fraction of the total hot electron energy, $F_{hot} = E_{hot} / E_{laser}$, are plotted versus laser power density (PW/cm^2). The T_{rad} was determined from the Dante 1 measurements. The F_{hot} was determined from the formalism in Ref [37]. For a Maxwellian distribution of electrons having a temperature, T_{hot} , the thick-target bremsstrahlung spectral intensity is approximated by $I = I_0 \exp(-h\nu / kT_{hot})$, which is determined by fitting the data recorded by the FFLEX. The total energy in hot electrons in joules, E_{hot} , can be expressed as, $E_{hot} = (I_{kT_{hot}} / 5 \times 10^{11}) (79 / Z)$. $I_{kT_{hot}}$ is the spectral intensity ($keV/(keV \ 4\pi \ sr)$) at kT_{hot} . Z is the atomic number of the target material. Power law fits for both the T_r and F_{hot} are given in the figure.

Also plotted as open points in Figure 17 are the measured data from the Ag halfraum targets discussed in this work. The Ag targets are less effective X-ray convertors than the Au halfraums. The difference is not as large as implied in the plots since the Au halfraum size was varied as well as the power density. The equivalent power density for the equivalent scale Au targets was not explored during these NIF shots. The 1.2 diameter Au halfraums were the closest in size to the Ag halfraums. These Au halfraums were heated with 16 kJ in 6 ns for a power of $1.4 PW/cm^2$. This was less power density than that used during the Ag halfraum target shots. The Au targets shot at the power density used for the Ag targets were smaller with a diameter of 0.31 mm and were heated with ~ 8.5 kJ in a 1.1 ns pulse. To compare the Ag targets to the NIF experiments, the target volume can be scaled. With a smaller volume, the energy density is $\sim (\pi (1mm)^2) / (2\pi * 0.31 \text{ mm} * 0.53 \text{ mm}) \sim 3x$. From Eq 1 in Ref [37], $T_r \sim (P_{laser}/V)^{0.25}$. V is the halfraum volume. The T_r of the smaller

Ag target should increase by ~ 1.3 bringing the value closer to, but not onto the best fit to the Au data (blue line).

The F_{hot} fraction from the Ag targets (open points) is also plotted in Figure 17. This F_{hot} needs to be corrected for the target volume. From equation 7 [37] $F_{hot} \sim 1 - (23 R^{3.2}) / (\tau P_{laser}^{0.83})$. τ is laser pulse time in ns, and P_{laser} is in TW. With a $\sim 3x$ decrease in volume, a Ag target would have an increase in the F_{hot} . The increase in F_{hot} is difficult to estimate from this formalism since it seems to break down for these size of targets as shown in Ref [37]. The increase in F_{hot} implies that the silver target has more plasma filling than an equivalent Au halfraum target. This may be a consequence of the more highly convergent spherical geometry of the Ag halfraums.

XI. CONCLUSION

The energetics of a novel silver halfraum target has been characterized in a set of four target shots at the NIF laser. These targets are designed to create a high-energy-density environment capable of driving pressure waves in air and solid surfaces for seismic studies. The objective was to characterize the target energetics and the laser coupling to the target using the existing NIF X-ray and optical diagnostics. The silver target was a 2 mm diameter ball with a 800 μm diameter LEH. The performance of targets with several different wall thickness of silver (8 to 16 μm) was characterized. The target was heated with ~ 10 kJ of energy in a 1 ns square laser pulse delivered by 4 beams from the NIF laser. The energy coupled into the targets was 0.85 to 0.88 of the total laser energy without the use of any phase plates to smooth the spatial profile of the beam. The coupling increased to 0.92 when 400 μm round spot CPPs were used to smooth each of the four lasers beams. The energy not coupled to the target was lost through X-ray radiation and optical backscatter (SRS and SBS) from the LEH. As expected, the different wall thickness had different levels of burn through emission. The thickest walled target ($\sim 15.9 \mu\text{m}$) had very little radiative losses. The thinnest walled targets ($\sim 8 \mu\text{m}$) radiated about 0.2 of the input energy in the X-ray.

XII. ACKNOWLEDGMENTS

This work was done under the auspices of the U.S. Department of Energy by Lawrence Livermore National Laboratory under Contract No. DE-AC52-07NA27344.

-
- [1] S. T. Prisbrey, H-S Park, B. A. Remington, R. Cavallo, M. May, S. M. Pollaine, R. Rudd, B. Maddox, A. Comley, L. Fried, K. Blobaum, R. Wallace, M. Wilson, D. Swift, J. Satcher, D. Kalantar, T. Perry, E. Giraldez, M. Farrell, A. Nikroo, *Phys. of Plasmas* **19** 056311 (2012).
 - [2] D. K. Bradley, J. H. Eggert, R. F. Smith, S. T. Prisbrey, D. G. Hicks, D. G. Braun, J. Biener, A. V. Hamza, R. E. Rudd, and G. W. Collins, *PRL* **102** 075503 (2009).
 - [3] K. B. Fournier, M. J. May, J. D. Colvin, J. O. Kane, M. Schneider, E. Dewald, C. A. Thomas, S. Compton, R. E. Marrs, J. Moody, E. Bond, P. Michel, J. H. Fisher, C. D. Newlander, and J. F. Davis, *Phys. of Plasmas* **17** 082701 (2010).
 - [4] S. W. Haan, J. D. Lindl, D. A. Callahan, D. S. Clark, J. D. Salmonson, B. A. Hammel, L. J. Atherton, R. C. Cook, M. J. Edwards, S. Glenzer, A. V. Hamza, S. P. Hatchett, M. C. Herrmann, D. E. Hinkel, D. D. Ho, H. Huang, O. S. Jones, J. Kline, G. Kyrala, O. L. Landen, B. J. MacGowan, M. M. Marinak, D. D. Meyerhofer, J. L. Milovich, K. A. Moreno, E. I. Moses, D. H. Munro, A. Nikroo, R. E. Olson, K. Peterson, S. M. Pollaine, J. E. Ralph, H. F. Robey, B. K. Spears, P. T. Springer, L. J. Suter, C. A. Thomas, R. P. Town, R. Vesey, S. V. Weber, H. L. Wilkens, and D. C. Wilson, *Phys of Plasmas* **18** 051001 2011
 - [5] J. D. Lindl, P. Amendt, R. L. Berger, S. G. Glendinning, S. H. Glenzer, S. W. Haan, R. L. Kauffman, O. L. Landen, and L. J. Suter, *Phys. of Plasmas* **11** 339 (2004).
 - [6] N. B. Meezan, L. J. Atherton, D. A. Callahan, E. L. Dewald, S. Dixit, E. G. Dzenitis, M. J. Edwards, C. A. Haynam, D. E. Hinkel, O. S. Jones, O. Landen, R. A. London, P. A. Michel, J. D. Moody, J. L. Milovich, M. B. Schneider, C. A. Thomas, R. P. J. Town, A. L. Warrick, S. V. Weber, K. Widmann, S. H. Glenzer, L. J. Suter, B. J. MacGowan, J. L. Kline, G. A. Kyrala and A. Nikroo, *Phys. of Plasmas* **17**, 056304 (2010).
 - [7] S. H. Glenzer, D. A. Callahan, A. J. MacKinnon, J. L. Kline, G. Grim, E. T. Alger, R. L. Berger, L. A. Bernstein, R. Betti, D. L. Bleuel, T. R. Boehly, D. K. Bradley, S. C. Burkhart, R. Burr, J. A. Caggiano, C. Castro, D. T. Casey, C. Choate, D. S. Clark, P. Celliers, C.

- J. Cerjan, G. W. Collins, E. L. Dewald, P. DiNicola, J. M. DiNicola, L. Divol, S. Dixit, T. Dppner, R. Dylla-Spears, E. Dzenitis, M. Eckart, G. Erbert, D. Farley, J. Fair, D. Fittinghoff, M. Frank, L. J. A. Frenje, S. Friedrich, D. T. Casey, M. Gatu Johnson, C. Gibson, E. Giraldez, V. Glebov, S. Glenn, N. Guler, S. W. Haan, B. J. Haid, B. A. Hammel, A. V. Hamza, C. A. Haynam, G. M. Heestand, M. Hermann, H. W. Hermann, D. G. Hicks, D. E. Hinkel, J. P. Holder, D. M. Holunda, J. B. Horner, W. W. Hsing, H. Huang, N. Izumi, M. Jackson, O. S. Jones, D. H. Kalantar, R. Kauffman, J. D. Kilkenny, R. K. Kirkwood, J. Klingmann, T. Kohut, J. P. Knauer, J. A. Koch, B. Kozioziemki, G. A. Kyrala, A. L. Kritcher, J. Kroll, K. La Fortune, L. Lagin, O. L. Landen, D. W. Larson, D. LaTray, R. J. Leeper, S. Le Pape, J. D. Lindl, R. Lowe-Webb, T. Ma, J. McNaney, A. G. MacPhee, T. N. Malsbury, E. Mapoles, C. D. Marshall, N. B. Meezan, F. Merrill, P. Michel, J. D. Moody, A. S. Moore, M. Moran, K. A. Moreno, D. H. Munro, B. R. Nathan, A. Nikroo, R. E. Olson, C. D. Orth, A. E. Pak, P. K. Patel, T. Parham, R. Petrasso, J. E. Ralph, H. Rinderknecht, S. P. Regan, H. F. Robey, J. S. Ross, M. D. Rosen, R. Sacks, J. D. Salmonson, R. Saunders, J. Sater, C. Sangster, M. B. Schneider, F. H. Sguin, M. J. Shaw, B. K. Spears, P. T. Springer, W. Stoeffl, L. J. Suter, C. A. Thomas, R. Tommasini, R. P. J. Town, C. Walters, S. Weaver, S. V. Weber, P. J. Wegner, P. K. Whitman, K. Widmann, C. C. Widmayer, C. H. Wilde, D. C. Wilson, B. Van Wonterghem, B. J. MacGowan, L. J. Atherton, M. J. Edwards, and E. I. Moses, *Phys. Plasmas* **19** 056318 (2012).
- [8] Hye-Sook Park, K. T. Lorenz, R. M. Cavallo, S. M. Pollaine, S. T. Prisbrey, R. E. Rudd, R. C. Becker, J. V. Bernier, and B. A. Remington, *Phys. Rev. Lett.* **104** 135504 (2010).
- [9] S. Glenzer et. al., *Plasma Physics and Controlled Fusion* **54** 4, 045013 (2010).
- [10] D. A. Callahan¹, N. B. Meezan, S. H. Glenzer, A. J. MacKinnon, L. R. Benedetti, D. K. Bradley, J. R. Celeste, P. M. Celliers, S. N. Dixit, T. Dppner, E. G. Dzentitis, S. Glenn, S. W. Haan, C. A. Haynam, D. G. Hicks, D. E. Hinkel, O. S. Jones, O. L. Landen, R. A. London, A. G. MacPhee, P. A. Michel, J. D. Moody, J. E. Ralph, H. F. Robey, M. D. Rosen, M. B. Schneider, D. J. Strozzi, L. J. Suter, R. P. J. Town, K. Widmann, E. A. Williams, M. J. Edwards, B. J. MacGowan, J. D. Lindl, L. J. Atherton, G. A. Kyrala, J. L. Kline, R. E. Olson, D. Edgell, S. P. Regan, A. Nikroo, H. Wilkins, J. D. Kilkenny and A. S. Moore, *Phys. of Plasmas* **19** 5, 056305 (2012).

- [11] D.E. Hinkel, M.B. Schneider, B.K. Young, A.B. Langdon, E.A. Williams, M.D. Rosen and L.J. Suter, Phys. Rev. Lett, **96** 195001 (2006).
- [12] M. B. Schneider, D. E. Hinkel, O. L. Landen, D. H. Froula, R. F. Heeter, A. B. Langdon, M. J. May, J. McDonald, J. S. Ross, M. S. Singh, L. J. Suter, K. Widmann, and B. K. Young, H. A. Baldis and C. Constantin, R. Bahr, V. Yu. Glebov, W. Seka, and C. Stoeckl, Phys. of Plasmas **13** 112701, (2006).
- [13] M.B. Schneider, D.E. Hinkel, S.J. Moon, S.B. Hansen, H.A. Baldis, C. Austrheim-Smith, G.V. Brown, K.M. Campbell, H.-K. Chung , K. Cone, C.G. Constantin, V.Yu. Glebov, J.P. Holder, G. Holland, D.L. James, A.B. Langdon, R.W. Lee, M.J. May, S. Roberts, J. Schein, J. Seely, W. Seka, R. Shepherd, M.S. Singh, C. Sorce, R.E. Turner, F. Weber, K. Widmann, B.K. Young, High Energy Density Physics **3** p 256-262 (2007).
- [14] D. E. Hinkel, M. B. Schneider, H. A. Baldis, G. Bonanno, D. E. Bower, K. M. Campbell, J. R. Celeste, S. Compton, R. Costa, E. L. Dewald, S. N. Dixit, M. J. Eckart, D. C. Eder, M. J. Edwards, A. Ellis, J. A. Emig, D. H. Froula, S. H. Glenzer, D. Hargrove, C. A. Haynam, R. F. Heeter, M. A. Henesian, J. P. Holder, G. Holtmeier, L. James, K. S. Jancaitis, D. H. Kalantar, J. H. Kamperschroer, R. L. Kauffman, J. Kimbrough, R. K. Kirkwood, A. E. Koniges, O. L. Landen, M. Landon, A. B. Langdon, F. D. Lee, B. J. MacGowan, A. J. Mackinnon, K. R. Manes, C. Marshall, M. J. May, J. W. McDonald, J. Menapace, E. I. Moses, D. H. Munro, J. R. Murray, C. Niemann, D. Pellinen, V. Rekow, J. A. Ruppe, J. Schein, R. Shepherd, M. S. Singh, P. T. Springer, C. H. Still, L. J. Suter, G. L. Tietbohl, R. E. Turner, B. M. Van Wonterghem, R. J. Wallace, A. Warrick, P. Watts, F. Weber, P. J. Wegner, E. A. Williams, B. K. Young, and P. E. Young, Phys. of Plasmas **12** 056305 (2005).
- [15] E.L. Dewald, O.L. Landel, L.J. Suter, J. Schein, J. Holder, K. Campbell, S.H. Glenzer, J.W. McDonald, C. Niemann, A.J. Mackinnon, M.S. Schneider, C. Haynam, D. Hinkel and A. Hammel. Phys. of Plasmas **12** 056315 (2006).
- [16] E. M. Giraldez, P. B. Mirkarimi, J. A. Emig, K. B. Fournier, H. Huang, J. S. Jaquez, E. C. Losbanos, M. J. May, J. D. Sain, M. E. Schoff, N. E. Teslich, M. T. Vu, R. J. Wallace, Fusion Science and Technology **63** 242 (2013).
- [17] M. Vandenboomgaerde, J. Bastian, A. Casner, D. Galmiche, J.-P. Jadaud, S. Laffite, S. Liberatore, G. Malinie, and F. Philippe, Phys. Rev. Lett. **99** 065004 (2007).
- [18] A. Nakumura and T. Mashimo, Jpn J. Appl. Phys **32** 4785 (1993).

- [19] K. Walter "NIF Experiments Track Weapons Effects to Improve Nuclear Forensics.", Science and Technology Review, Editor A.J. Simon, Sept (2013) LLNL-TR-52000-13-9.
- [20] W. L. Kruer, The Physics of Laser Plasma Interactions (Westview, Boulder, CO), (2003).
- [21] E. L. Dewald, K. M. Campbell, R. E. Turner, J. P. Holder, O. L. Landen, S. H. Glenzer, R. L. Kauffman, L. J. Suter, M. Landon, M. Rhodes, and D. Lee, Rev. Sci. Instrum. **75** 3759 (2004).
- [22] M. Landon, J. Koch, S. Alvarez, P. Bell, F. Lee, and J. Moody, Rev. Sci. Instrum. **72** 698 (2001).
- [23] D. H. Froula, D. Bower, M. Chrisp, S. Grace, J. H. Kamperschroer, T. M. Kelleher, R. K. Kirkwood, B. MacGowan, T. McCarville, N. Sewall, F. Y. Shimamoto, S. J. Shiromizu, B. Young, and S. H. Glenzer, Rev. Sci. Instrum. **75** 4168 (2004).
- [24] A. J. Mackinnon, T. McCarville, K. Piston, C. Niemann, G. Jones, I. Reinbachs, R. Costa, J. Celeste, G. Holtmeier, R. Griffith, R. Kirkwood, B. MacGowan, S. H. Glenzer, and M. R. Latta, Rev. Sci. Instrum. **75** 4183 (2004).
- [25] P J Wegner, J M Auerbach, M W Bowers, S N Dixit, G V Erbert, G M Heestand, M A Henesian, M R Hermann, K S Jancaitis, K R Manes, C D Marshall, N C Mehta, J Menapace, E Moses, J R Murray, M C Nostrand, C D Orth, R Patterson, R A Sacks, M J Shaw, M Spaeth, S B Sutton, W H Williams, C C Widmayer, R K White, S T Yang, B M Van Wonerghem, Applied Optics **46** 3276-3303 (2007).
- [26] J. Orloff, L. W. Swanson, and M. Utlaut, J. Vac. Sci. Technol. B **14** 3759 (1996).
- [27] <http://www.xradia.com>
- [28] G. Zimmerman and W. Kruer, Comments Plasma Phys. Controlled Fusion **2**, 51 (1975)
- [29] J. A. Harte, W. E. Alley, D. S. Bailey, J. L. Eddleman, G. B. Zimmerman, LLNL technical report UCRL-LR-105821-96-4 (1996).
- [30] J. D. Colvin, K. B. Fournier, M. J. May, and H. A. Scott, Phys. Plasmas **17** 073111 (2010).
- [31] J. D. Colvin, K. B. Fournier, J. Kane, S. Langer, M. J. May, and H. A. Scott, High Energy Density Phys. **7** 263 (2011).
- [32] H. Scott and S. Hansen, High Energy Density Physics **6** 39-47 (2010).
- [33] H. N. Komblum, R. L. Kauffman, and J. A. Smith, Rev. Sci. Instrum. **57** 2179 (1986).
- [34] M. J. May, K. Widmann, C. Sorce, H.-S. Park, and M. Schneider, Rev. Sci. Instrum. **8**, 10E505 (2010).

- [35] J. W. McDonald, R. L. Kauffman, J. R. Celeste, M. A. Rhodes, F. D. Lee, L. J. Suter, A. P. Lee, J. M. Foster, and G. Slark, *Rev. Sci. Instrum.* **75**, 3753 (2004).
- [36] C. L. Wang, *Rev. Sci. Instrum.* **52** 1317 (1981).
- [37] J. W. McDonald, L. J. Suter, O. L. Landen, J. M. Foster,^a J. R. Celeste, J. P. Holder, E. L. Dewald, M. B. Schneider, D. E. Hinkel, R. L. Kauffman, L. J. Atherton, R. E. Bonanno, S. N. Dixit, D. C. Eder, C. A. Haynam, D. H. Kalantar, A. E. Koniges, F. D. Lee, B. J. MacGowan, K. R. Manes, D. H. Munro, J. R. Murray, M. J. Shaw, R. M. Stevenson,^a T. G. Parham, B. M. Van Wonterghem, R. J. Wallace, P. J. Wegner, P. K. Whitman, B. K. Young, B. A. Hammel, and E. I. Moses *Phys. of Plasmas*. **13** 032703 (2006).
- [38] E. L. Dewald, L. J. Suter, O. L. Landen, J. P. Holder, J. Schein, F. D. Lee, K. M. Campbell, F. A. Weber, D. G. Pellinen, M. B. Schneider, J. R. Celeste, J. W. McDonald, J. M. Foster, C. Niemann, A. J. Mackinnon,¹ S. H. Glenzer, B. K. Young, C. A. Haynam, M. J. Shaw, R. E. Turner, D. Froula, R. L. Kauffman, B. R. Thomas, L. J. Atherton, R. E. Bonanno, S. N. Dixit, D. C. Eder, G. Holtmeier, D. H. Kalantar, A. E. Koniges, B. J. MacGowan, K. R. Manes, D. H. Munro, J. R. Murray, T. G. Parham, K. Piston, B. M. Van Wonterghem, R. J. Wallace, P. J. Wegner, P. K. Whitman, B. A. Hammel, and E. I. Moses, *Phys. Rev. Lett.* **95** 215004 (2005).

TABLE I. Configuration of Dante 1. Columns are the channel number, the number of each type of filter, the filters present in the channel, present, the type of XRD used, a soft x-ray mirror with angle of grazing incidence if present, the energy range over which that channel had sensitivity, and the solid angle subtended by that channel.

Channel	Filter	Qty	XRD	Mirror	Energy Range	Energy Range	Solid angle
					Center (eV)	Width (eV)	
1	Al 0.8 μm	2	Cr	7° B ₄ C	61.2	12.6	6.026
2	B 0.2 μm + CH 0.4 μm	4	Al	5° amorphous C	167.7	26.4	5.929
3	Lexan 2.0 μm	2	Al	3.5° SiO ₂	249.3	45.6	5.786
4	V 1.0 μm	2	Ni	2.5° SiO ₂	474.4	50.6	5.603
5	Co 1.0 μm + Co 0.4 μm + CH 0.2 μm	1	Cr	-	716.0	84.8	6.514
6	Cu 1.0 μm	1	Cr	-	864.2	92.6	6.514
7	Mg 5.0 μm + Zn 1.0 μm + CH 0.1 μm	1	Ni	-	943.4	97.2	6.514
8	Mg 11 μm	2	Ni	-	1182.8	158.4	6.514
9	Al 10 μm	2	Ni	-	1431.4	172.4	6.514
10	Si 10 μm	1	Al	-	1700.9	161.1	6.514
11	Fe 1.25 μm + Cr 0.65 μm + Parylene 5.0 μm	1	Al	-	3417.0	683.4	6.514
12	Saran 22 μm	2	Al	-	2462.8	474.0	6.514
13	Ag 2.2 μm	1	Al	-	2767.0	553.4	6.514
14	Ti 13 μm	1	Al	-	3698.3	739.6	6.514
15	Mn 13.2 μm + Ni 1.8 μm	1	Ni	-	5187.7	1037.5	6.514
16	Ni 10 μm	1	Ni	-	6676.5	1335.3	6.514
17	Sc 0.8 μm + Ti 0.5 μm	1	Al	2.5° SiO ₂	348.9	61.6	5.603
18	Al 250 μm	1	Ni	-	14479.8	2895.9	17.73

TABLE II. Configuration of Dante 2. Columns are the channel number, the number of each type of filter, the filters present in the channel, present, the type of XRD used, a soft x-ray mirror with angle of grazing incidence if present, the energy range over which that channel had sensitivity, and the solid angle subtended by that channel.

Channel	Filter	Qty	XRD	Mirror	Energy Range	Energy Range	Solid angle
					Center (eV)	Width (eV)	
1	Al 10 μm	1	Ni	-	1337.6	267.5	6.514
2	Mg 11 μm	1	Ni	-	1109.8	221.9	6.514
3	Al 0.8 μm	1	Cr	7° B ₄ C	43.7	33.9	6.026
4	Al 0.8 μm	2	Cr	7° B ₄ C	61.3	12.7	6.026
5	B 0.2 μm + CH 0.4 μm	1	Al	5° amorphous C	149.9	47.5	5.929
6	B 0.2 μm + CH 0.4 μm	2	Al	5° amorphous C	155.0	41.6	5.929
7	Cu 1.0 μm	1	Al	-	822.8	148.2	6.514
8	Lexan 2.0 μm	1	Al	3.5° SiO ₂	227.6	70.4	5.786
9	Lexan 2.0 μm	2	Al	2.5° Vitreous C	246.5	44.4	1.525
10	Ti 0.5 μm	1	Al	2.5° SiO ₂	369.6	94.7	1.525
11	Ti 0.5 μm	2	Ni	2.5° SiO ₂	394.3	77.6	1.525
12	Si 10 μm	1	Al	-	1700.7	157.5	6.514
13	Co 1.0 μm	1	Cr	-	690.3	116.9	6.514
14	Co 1.0 μm	1	Cr	-	689.8	117.4	6.514
15	Mg 5.0 μm + Zn 1.0 μm + CH 0.1 μm	1	Ni	-	943.5	97.7	6.514
16	Cu 1.0 μm	1	Al	-	810.0	158.9	6.514
17	Mg 5.0 μm + Zn 1.0 μm + CH 0.1 μm	1	Ni	-	942.2	97.9	6.514
18	Fe 1.25 μm + Parylene 5.0 μm + Cr 0.65 μm	1	Al	-	3388.7	677.7	6.514

TABLE III. Energy partitioning for the silver laser targets.

Shot		N110313-001-999	N110313-002-999	N120129-002-999	N120129-003-999
Target		A-B-01	A-A-01	A-B-04	A-B-02
Target Mandrille		Al	Al	CH	Al
Target Wall (μm)		12 \pm 1.2	15.9 \pm 1.3	8.1 \pm 0.9	8.0 \pm 0.9
Laser Energy (kJ)		10.12 \pm 0.05	10.25 \pm 0.51	9.53 \pm 0.48	9.29 \pm 0.46
CPPs		No	No	Yes	Yes
Spot Size		defocused 400 μm	defocused 400 μm	400 μm	400 μm
Peak T_r (eV)		239	212	220	215
Dante 1 (0-10ns)	Radiant Energy (J/sr)	650 \pm 50	422 \pm 30	588 \pm 45	487 \pm 35
	Energy (J)	787 \pm 60	511 \pm 36	711 \pm 55	589 \pm 42
Drive Losses	(Fraction)	0.077 \pm 0.007	0.049 \pm 0.004	0.075 \pm 0.007	0.063 \pm 0.006
Backscatter		31B (30°)	31B (30°)	31B (30°)	31B (30°)
		SRS SBS	SRS SBS	SRS SBS	SRS SBS
	FABs+NBI (J)	527 \pm 110 130 \pm 40	460 \pm 100 280 \pm 60	15. \pm 7. 20. \pm 10.	177 \pm 40. 10. \pm 5
Total Backscatter (J)		657 \pm 120	740 \pm 120	35 \pm 12	190 \pm 40
FFLEX (> 10 keV)	Radiant Energy (J/sr)	1.00	1.56	3.77	3.73
	Energy (J)	12.6	19.6	47.3	46.9
	Fit T_e Low (keV)	3.15	2.60	2.80	2.65
	Fit T_e High (keV)	35.4	37.7	43.0	39.3
Other Losses (Backscatter and FFLEX)	(Fraction)	0.066 \pm 0.013	0.074 \pm 0.013	0.0091 \pm 0.0031	0.026 \pm 0.005
Total Energy Coupling	(Fraction)	0.86 \pm 0.015	0.88 \pm 0.014	0.92 \pm 0.008	0.92 \pm 0.008
Dante 2	Radiant Energy (J/sr)	$> 10.44\pm 1.$	$> 0.463\pm 0.3$	231 \pm 20	195 \pm 17
	Energy (J)	$> 91.0\pm 8.$	$> 4.0\pm 2.6$	1990 \pm 175	1690 \pm 148
Total X-ray Burn-through	(Fraction)	$> 0.009\pm 0.0009$	$> 0.0004\pm 0.0003$	0.22 \pm 0.02	0.18 \pm 0.02
Coupled into K.E.	(Fraction)	0.85 \pm 0.015	0.88 \pm 0.013	0.69 \pm 0.02	0.73 \pm 0.02

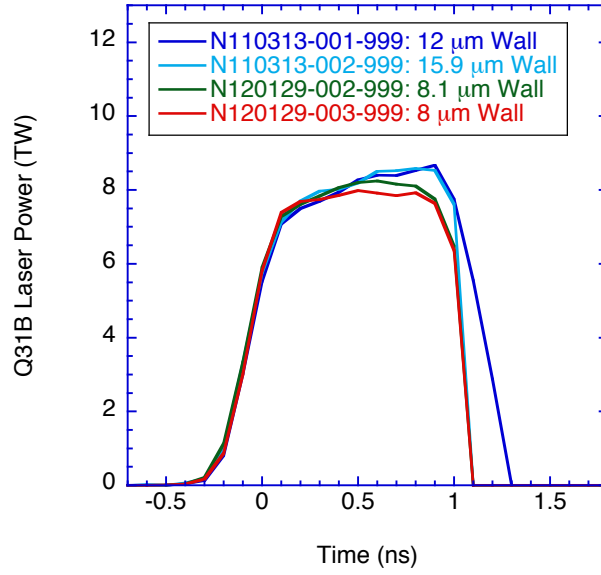


FIG. 1. Measured laser power for NIF shots N110313-001-999, N110313-002-999, N120129-002-999 and N120129-003-999.



FIG. 2. Silver halfraum target photo before mounting (left) and alignment image (right) before the NIF shot.

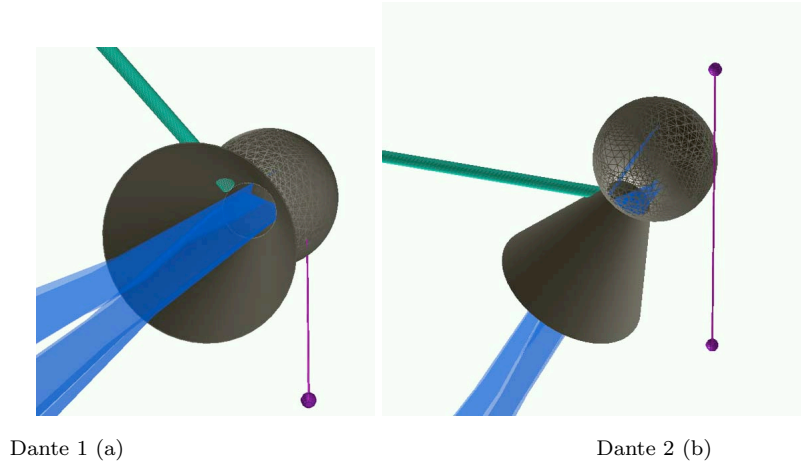


FIG. 3. Views of the halfraum target see by the Dante 1 in (a), Dante 2 in (b) showing the mounting stalk (green), alignment features (purple) and the NIF laser beams (blue).

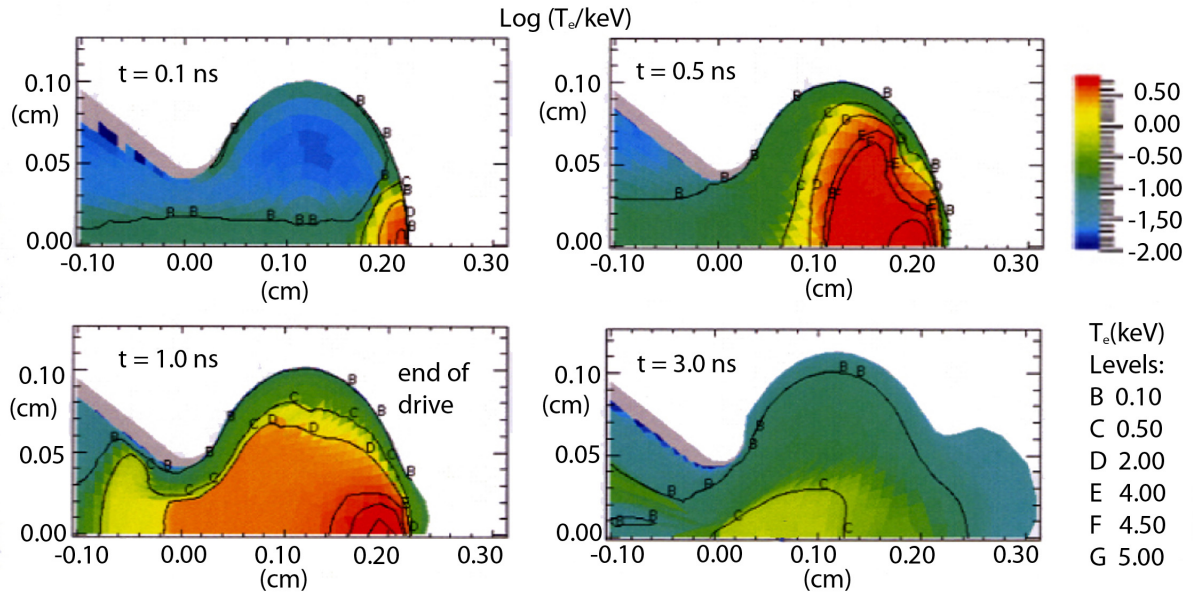


FIG. 4. Electron temperature simulations from LASNEX

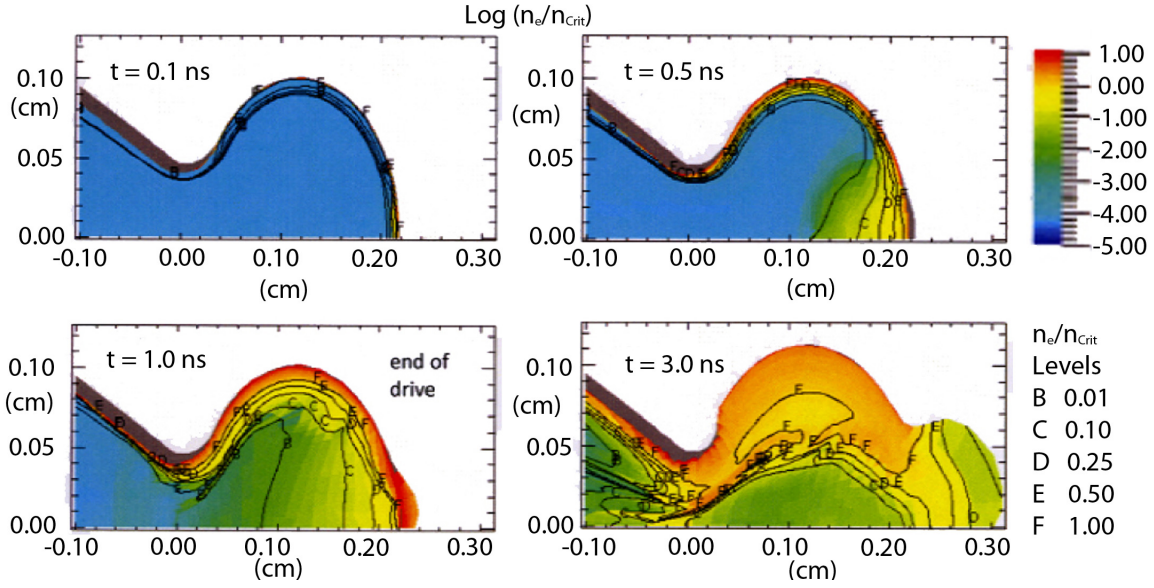


FIG. 5. Electron density simulations from LASNEX

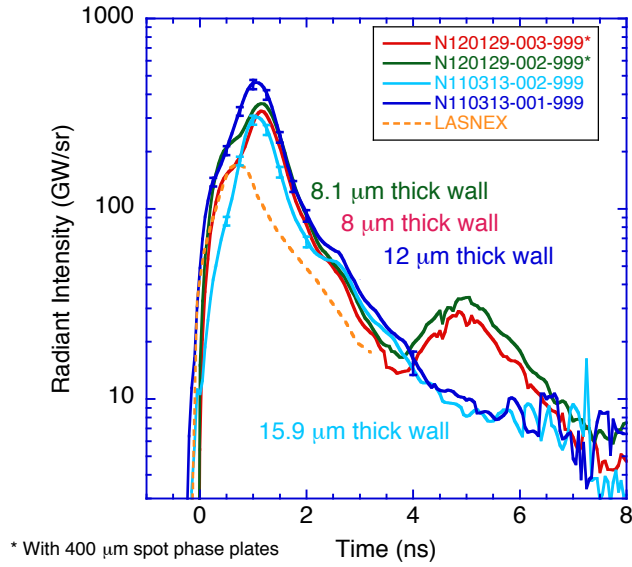


FIG. 6. Reconstructed radiant intensity from the laser entrance hole as a function of time for Dante 1 for all four spherical Ag targets.

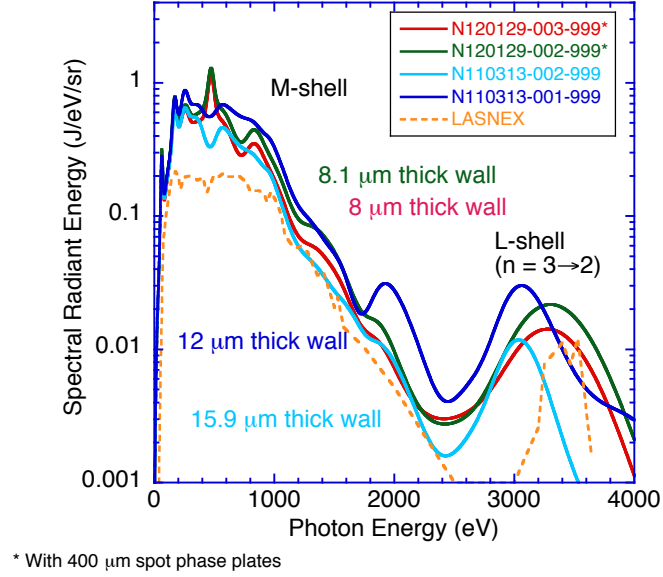


FIG. 7. Reconstructed spectral radiant intensity as a function of photon energy for Dante 1 for all four thin walled Ag targets.

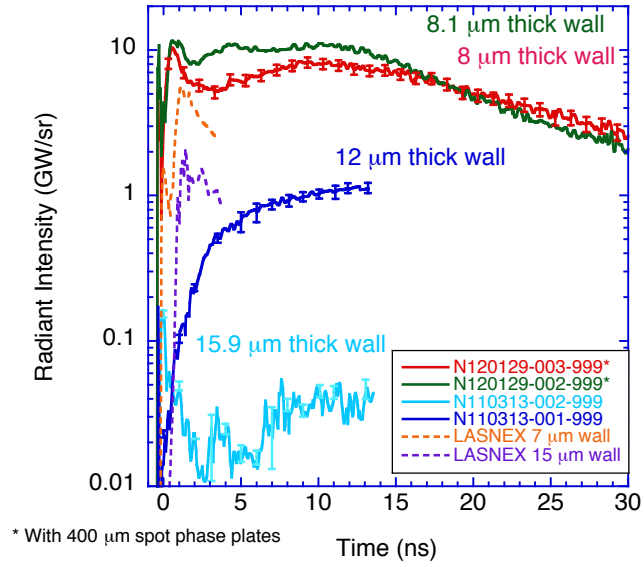


FIG. 8. Reconstructed radiant intensity as a function of time for Dante 2 for all four thin walled Ag targets.

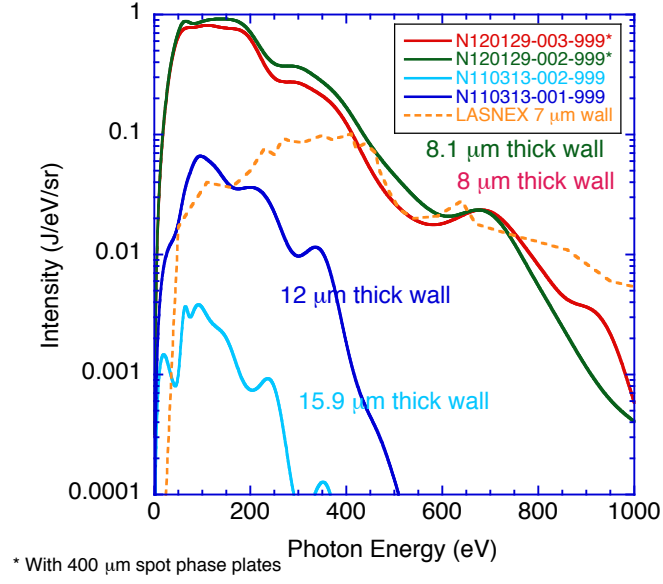


FIG. 9. Reconstructed spectral radiant intensity as a function of photon energy for Dante 2 for all four thin walled Ag targets.

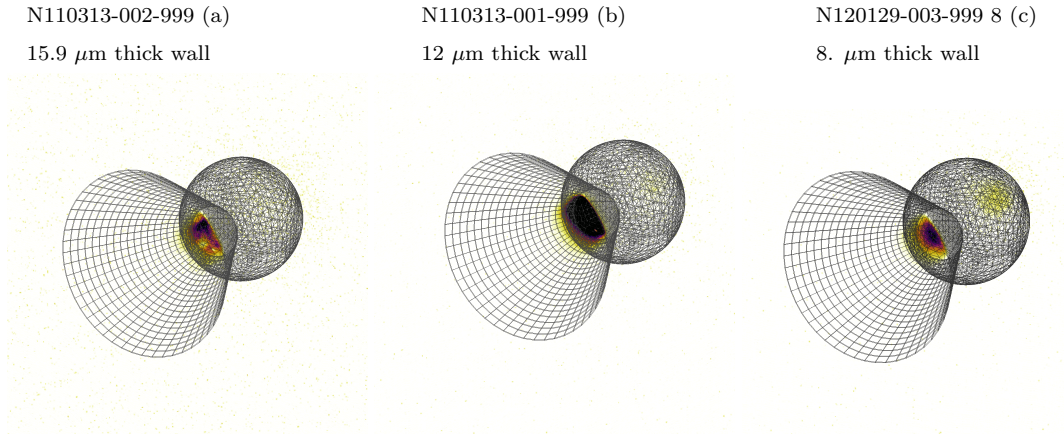


FIG. 10. Images from the SXI-L (laser drive view) for the 12 μm (a) and 15.9 μm (b) and 8 μm (c) thick walled Ag targets.

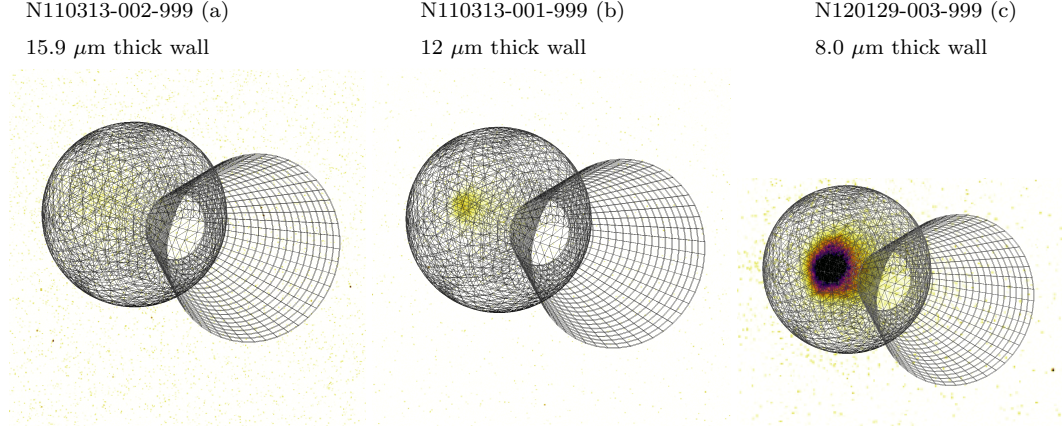


FIG. 11. Images from the SXI-U (wall view) for the 12 μm (a) and 15.9 μm (b) and 8.0 μm (c) thick walled Ag targets. Filtering: 5 μm Ti /2 μm Cu/1 μm Polyimide.

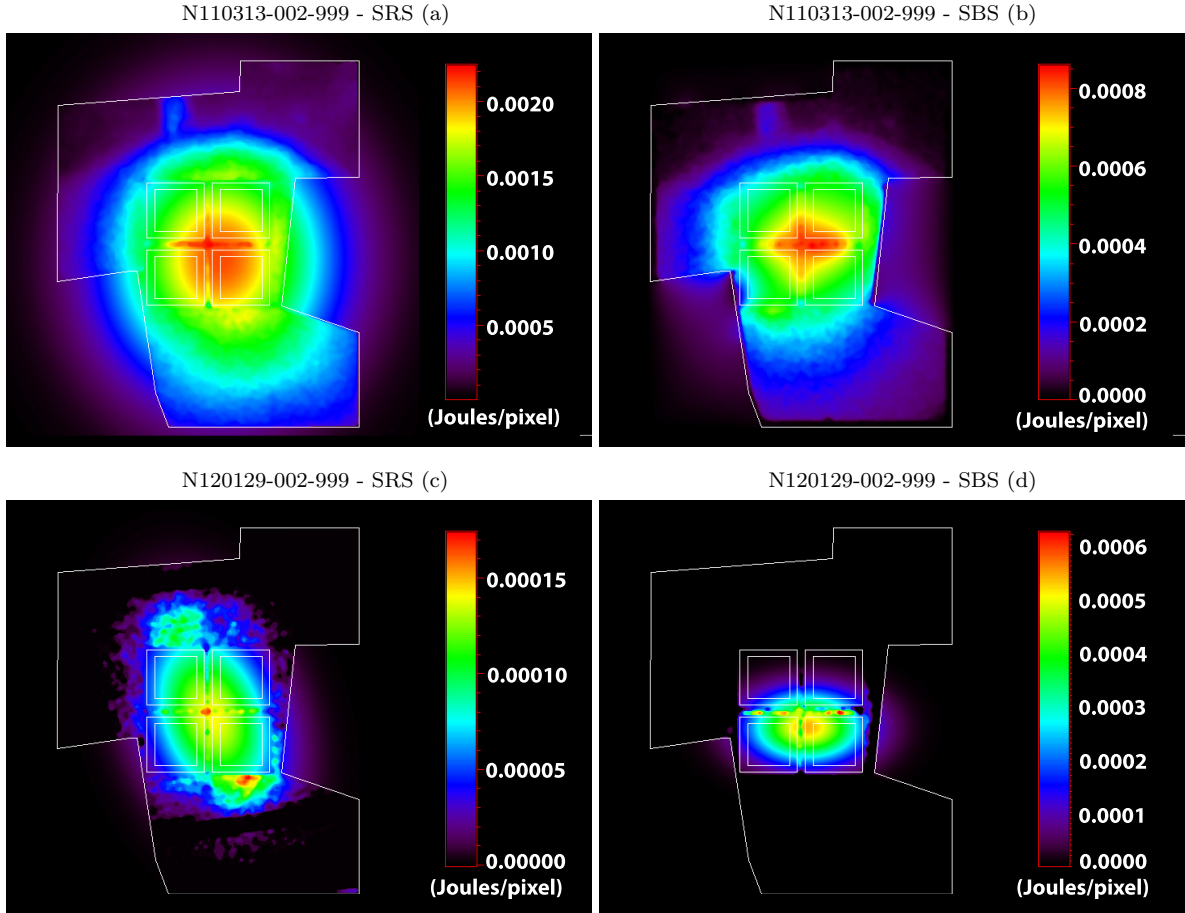


FIG. 12. SRS (a) and SBS (b) Images from the Near Beam Imager (NBI) for shots N110313-002-999 (without CCPs) and N120129-002-999 (with CCPs). Each camera pixel is 20 μm x 20 μm

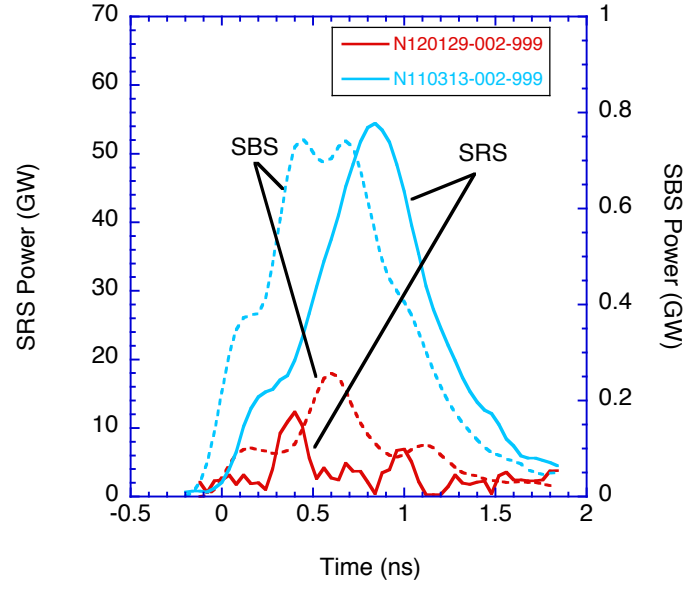


FIG. 13. Measured SRS and SBS power for NIF shots N110313-002-999 (without CCPs) and N120129-002-999 (with CCPs)

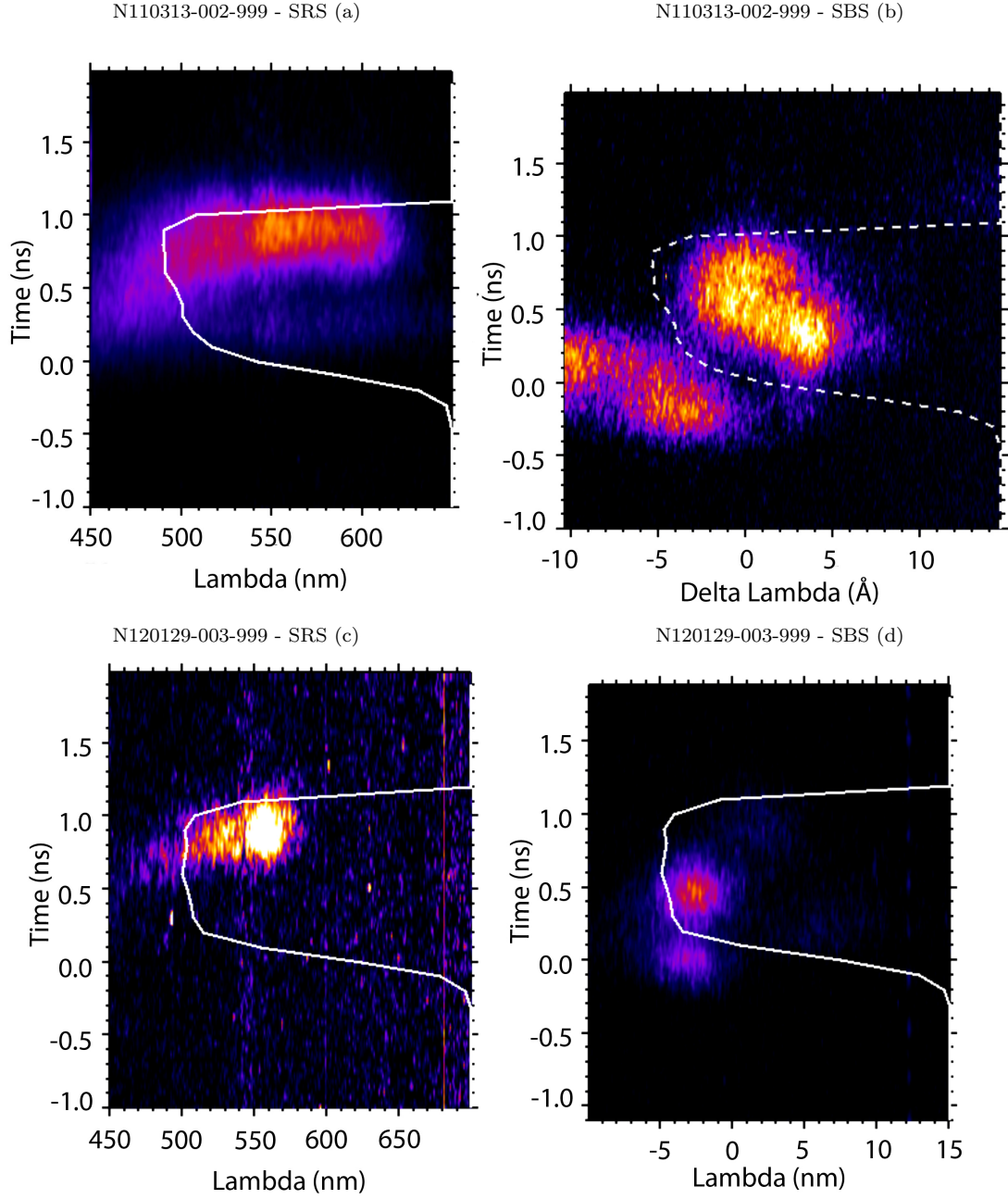


FIG. 14. SRS (a) and SBS (b) streaked spectra for shots N110313-002-999 (without CCPs) and N120129-003-999 (with CCPs).

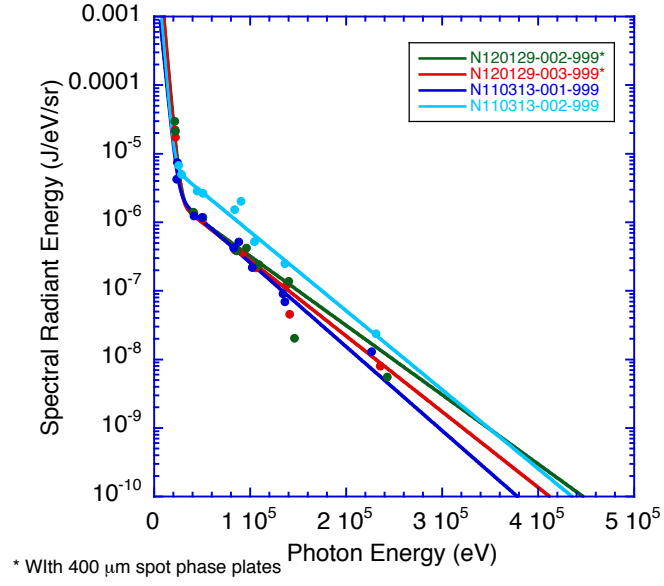


FIG. 15. Time integrated FFLEX spectra.

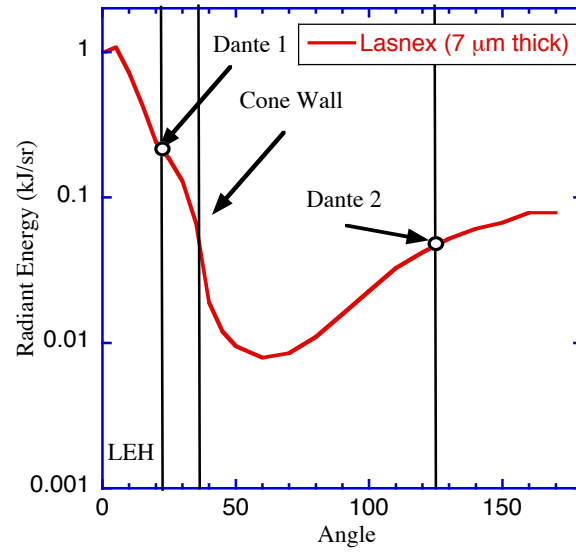


FIG. 16. Predicted angular X-ray emission from LASNEX modeling.

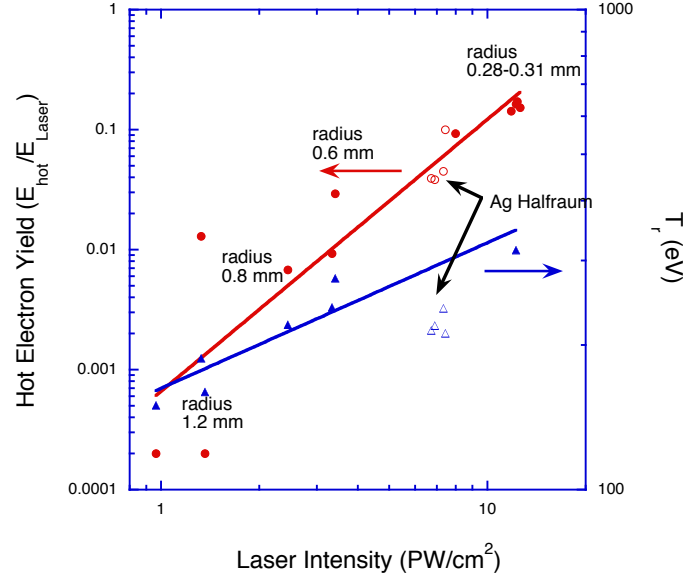


FIG. 17. Comparison of the T_{rad} and F_{hot} Ref [37, 38] for previous NIF Au Halfraum targets to the Ag Halfraum targets in the current work. The lines are power law fits to the data.